Research Article | Vol. 26, No. 2 | 22 Jan 2018 | OPTICS EXPRESS 905
Optics EXPRESS

Spin-controlled twisted laser beams: intra-cavity multi-tasking geometric phase metasurfaces

RONEN CHRIKI,[1,3] ELHANAN MAGUID,[2,3] CHENE TRADONSKY,[1] VLADIMIR KLEINER,[2] ASHER A. FRIESEM,[1] NIR DAVIDSON,[1] AND EREZ HASMAN[2,*]

[1]*Weizmann Institute of Science, Department of Physics of Complex Systems, Rehovot 7610001, Israel*
[2]*Micro and Nanooptics Laboratory, Faculty of Mechanical Engineering and Russell Berrie Nanotechnology Institute, Technion – Israel Institute of Technology, Haifa 3200003, Israel*
[3]*These authors contributed equally*
[*]*mehasman@technion.ac.il*

Abstract: Novel multi-tasking geometric phase metasurfaces were incorporated into a modified degenerate cavity laser as an output coupler to efficiently generate spin-dependent twisted light beams of different topologies. Multiple harmonic scalar vortex laser beams were formed by replacing the laser output coupler with a shared-aperture metasurface. A variety of distinct wave functions were obtained with an interleaving approach – random interspersing of geometric phase profiles within shared-aperture metasurfaces. Utilizing the interleaved metasurfaces, we generated vectorial vortices by coherently superposing of scalar vortices with opposite topological charges and spin states. We also generated multiple partially coherent vortices by incorporating harmonic response metasurfaces. The incorporation of the metasurface platforms into a laser cavity opens a pathway to novel types of nanophotonic functionalities and enhanced light-matter interactions, offering exciting new opportunities for light manipulation.

OCIS codes: (140.0140) Lasers and laser optics; (140.3300) Laser beam shaping; (350.1370) Berry's phase; (160.3918) Metamaterials; (050.6624) Subwavelength structures.

References and links

1. W. Koechner and M. Bass, *Solid-State Lasers: A Graduate Text* (Springer Science & Media, 2003).
2. E. Maguid, I. Yulevich, D. Veksler, V. Kleiner, M. L. Brongersma, and E. Hasman, "Photonic spin-controlled multifunctional shared-aperture antenna array," Science **352**(6290), 1202–1206 (2016).
3. K. Y. Bliokh, F. J. Rodríguez-Fortuño, F. Nori, and A. V. Zayats, "Spin-orbit interactions of light," Nat. Photonics **9**(12), 796–808 (2015).
4. K. Y. Bliokh and F. Nori, "Transverse and longitudinal angular momenta of light," Phys. Rep. **592**, 1–38 (2015).
5. J. Wynne, "Generation of the rotationally symmetric TE01 and TM01 from a wavelength-tunable laser," IEEE J. Quantum Electron. **10**, 125–127 (1974).
6. R. Oron, S. Blit, N. Davidson, A. A. Friesem, Z. Bomzon, and E. Hasman, "The formation of laser beams with pure azimuthal or radial polarization," Appl. Phys. Lett. **77**(21), 3322–3324 (2000).
7. R. Oron, N. Davidson, A. A. Friesem, and E. Hasman, "Transverse mode shaping and selection in laser resonators," Prog. Opt. **42**, 325–386 (2001).
8. L. Shimshi, A. A. Ishaaya, V. Ekhouse, N. Davidson, and A. A. Friesem, "Passive intra-cavity phase locking of laser channels," Opt. Commun. **263**(1), 60–64 (2006).
9. A. A. Ishaaya, N. Davidson, and A. A. Friesem, "Passive Laser Beam Combining With Intracavity Interferometric Combiners," IEEE J. Sel. Top. Quantum Electron. **15**(2), 301–311 (2009).
10. M. Nixon, O. Katz, E. Small, Y. Bromberg, A. A. Friesem, Y. Silberberg, and N. Davidson, "Real-time wavefront shaping through scattering media by all-optical feedback," Nat. Photonics **7**(11), 919–924 (2013).
11. Y. Ye, Z. J. Wong, X. Lu, X. Ni, H. Zhu, X. Chen, Y. Wang, and X. Zhang, "Monolayer excitonic laser," Nat. Photonics **9**(11), 733–737 (2015).
12. D. Naidoo, F. S. Roux, A. Dudley, I. Litvin, B. Piccirillo, L. Marrucci, and A. Forbes, "Controlled generation of higher-order Poincaré sphere beams from a laser," Nat. Photonics **10**(5), 327–332 (2016).
13. S. Ngcobo, I. Litvin, L. Burger, and A. Forbes, "A digital laser for on-demand laser modes," Nat. Commun. **4**, 2289 (2013).
14. P. Miao, Z. Zhang, J. Sun, W. Walasik, S. Longhi, N. M. Litchinitser, and L. Feng, "Orbital Angular Momentum Microlaser," Science **353**(6298), 464–467 (2016).

#313980 https://doi.org/10.1364/OE.26.000905
Journal © 2018 Received 22 Nov 2017; revised 14 Dec 2017; accepted 27 Dec 2017; published 9 Jan 2018

Optics EXPRESS

15. L. Xu, D. Chen, T. Itoh, J. L. Reno, and B. S. Williams, "Focusing metasurface quantum-cascade laser with a near diffraction-limited beam," Opt. Express **24**(21), 24117–24128 (2016).
16. Z. J. Wong, Y. Xu, J. Kim, K. O'Brien, Y. Wang, L. Feng, and X. Zhang, "Lasing and anti-lasing in a single cavity," Nat. Photonics **7**(10), 796–801 (2016).
17. S. Knitter, C. Liu, B. Redding, M. K. Khokha, M. A. Choma, and H. Cao, "Coherence switching of a degenerate VECSEL for multimodality imaging," Optica **3**(4), 403 (2016).
18. P. Lalanne, S. Astilean, P. Chavel, E. Cambril, and H. Launois, "Blazed binary subwavelength gratings with efficiencies larger than those of conventional échelette gratings," Opt. Lett. **23**(14), 1081–1083 (1998).
19. Z. Bomzon, V. Kleiner, and E. Hasman, "Pancharatnam-Berry phase in space-variant polarization-state manipulations with subwavelength gratings," Opt. Lett. **26**(18), 1424–1426 (2001).
20. Z. Bomzon, G. Biener, V. Kleiner, and E. Hasman, "Space-variant Pancharatnam-Berry phase optical elements with computer-generated subwavelength gratings," Opt. Lett. **27**(13), 1141–1143 (2002).
21. G. Biener, A. Niv, V. Kleiner, and E. Hasman, "Formation of helical beams by use of Pancharatnam-Berry phase optical elements," Opt. Lett. **27**(21), 1875–1877 (2002).
22. L. Marrucci, C. Manzo, and D. Paparo, "Optical spin-to-orbital angular momentum conversion in inhomogeneous anisotropic media," Phys. Rev. Lett. **96**(16), 163905 (2006).
23. N. Yu, P. Genevet, M. A. Kats, F. Aieta, J. P. Tetienne, F. Capasso, and Z. Gaburro, "Light Propagation with Phase Discontinuities: Generalized Laws of Reflection and Refraction," Science **334**(6054), 333–337 (2011).
24. X. Ni, N. K. Emani, A. V. Kildishev, A. Boltasseva, and V. M. Shalaev, "Broadband Light Bending with Plasmonic Nanoantennas," Science **335**(6067), 427 (2012).
25. A. Pors, M. G. Nielsen, and S. I. Bozhevolnyi, "Broadband plasmonic half-wave plates in reflection," Opt. Lett. **38**(4), 513–515 (2013).
26. A. Pors, O. Albrektsen, I. P. Radko, and S. I. Bozhevolnyi, "Gap plasmon-based metasurfaces for total control of reflected light," Sci. Rep. **3**(1), 2155 (2013).
27. J. Sun, X. Wang, T. Xu, Z. A. Kudyshev, A. N. Cartwright, and N. M. Litchinitser, "Spinning Light on the Nanoscale," Nano Lett. **14**(5), 2726–2729 (2014).
28. D. Lin, P. Fan, E. Hasman, and M. L. Brongersma, "Dielectric gradient metasurface optical elements," Science **345**(6194), 298–302 (2014).
29. A. Arbabi, Y. Horie, M. Bagheri, and A. Faraon, "Dielectric metasurfaces for complete control of phase and polarization with subwavelength spatial resolution and high transmission," Nat. Nanotechnol. **10**(11), 937–943 (2015).
30. G. Zheng, H. Mühlenbernd, M. Kenney, G. Li, T. Zentgraf, and S. Zhang, "Metasurface holograms reaching 80% efficiency," Nat. Nanotechnol. **10**(4), 308–312 (2015).
31. K. E. Chong, I. Staude, A. James, J. Dominguez, S. Liu, S. Campione, G. S. Subramania, T. S. Luk, M. Decker, D. N. Neshev, I. Brener, and Y. S. Kivshar, "Polarization-Independent Silicon Metadevices for Efficient Optical Wavefront Control," Nano Lett. **15**(8), 5369–5374 (2015).
32. Q. Wang, E. T. F. Rogers, B. Gholipour, C. Wang, G. Yuan, J. Teng, and N. I. Zheludev, "Optically reconfigurable metasurfaces and photonic devices based on phase change materials," Nat. Photonics **10**(1), 60–65 (2016).
33. M. V. Berry, "The Adiabatic Phase and Pancharatnam's Phase for Polarized Light," J. Mod. Opt. **34**(11), 1401–1407 (1987).
34. K. Y. Bliokh, Y. Gorodetski, V. Kleiner, and E. Hasman, "Coriolis Effect in Optics: Unified Geometric Phase and Spin-Hall Effect," Phys. Rev. Lett. **101**(3), 030404 (2008).
35. R. L. Haupt, "Interleaved thinned linear arrays," IEEE Trans. Antenn. Propag. **53**(9), 2858–2864 (2005).
36. I. E. Lager, C. Trampuz, M. Simeoni, and L. P. Ligthart, "Interleaved Array Antennas for FMCW Radar Applications," IEEE Trans. Antenn. Propag. **57**(8), 2486–2490 (2009).
37. H. Dammann and K. Görtler, "High-efficiency in-line multiple imaging by means of multiple phase holograms," Opt. Commun. **3**(5), 312–315 (1971).
38. F. Gori, M. Santarsiero, S. Vicalvi, R. Borghi, G. Cincotti, E. Di Fabrizio, and M. Gentili, "Analytical derivation of the optimum triplicator," Opt. Commun. **157**(1-6), 13–16 (1998).
39. M. Nixon, E. Ronen, A. A. Friesem, and N. Davidson, "Observing geometric frustration with thousands of coupled lasers," Phys. Rev. Lett. **110**(18), 184102 (2013).
40. M. Nixon, B. Redding, A. A. Friesem, H. Cao, and N. Davidson, "Efficient method for controlling the spatial coherence of a laser," Opt. Lett. **38**(19), 3858–3861 (2013).
41. R. Chriki, M. Nixon, V. Pal, C. Tradonsky, G. Barach, A. A. Friesem, and N. Davidson, "Manipulating the spatial coherence of a laser source," Opt. Express **23**(10), 12989–12997 (2015).
42. D. M. Palacios, I. D. Maleev, A. S. Marathay, and G. A. Swartzlander, Jr., "Spatial correlation singularity of a vortex field," Phys. Rev. Lett. **92**(14), 143905 (2004).
43. G. A. Swartzlander, Jr. and R. I. Hernandez-Aranda, "Optical Rankine vortex and anomalous circulation of light," Phys. Rev. Lett. **99**(16), 163901 (2007).
44. Y. Yang, M. Mazilu, and K. Dholakia, "Measuring the orbital angular momentum of partially coherent optical vortices through singularities in their cross-spectral density functions," Opt. Lett. **37**(23), 4949–4951 (2012).
45. N. B. Simpson, K. Dholakia, L. Allen, and M. J. Padgett, "Mechanical equivalence of spin and orbital angular momentum of light: an optical spanner," Opt. Lett. **22**(1), 52–54 (1997).
46. M. S. Soskin and M. V. Vasnetsov, "*Singular optics*," Prog. Opt. **42**, 219–276 (2001).

Optics EXPRESS

47. J. Wang, J. Yang, I. M. Fazal, N. Ahmed, Y. Yan, H. Huang, Y. Ren, Y. Yue, S. Dolinar, M. Tur, and A. E. Willner, "Terabit free-space data transmission employing orbital angular momentum multiplexing," Nat. Photonics **6**(7), 488–496 (2012).
48. A. Niv, G. Biener, V. Kleiner, and E. Hasman, "Manipulation of the Pancharatnam phase in vectorial vortices," Opt. Express **14**(10), 4208–4220 (2006).
49. R. Dorn, S. Quabis, and G. Leuchs, "Sharper Focus for a Radially Polarized Light Beam," Phys. Rev. Lett. **91**(23), 233901 (2003).
50. V. Shvedov, A. R. Davoyan, C. Hnatovsky, N. Engheta, and W. Krolikowski, "A long-range polarization-controlled optical tractor beam," Nat. Photonics **8**(11), 846–850 (2014).
51. M. P. Backlund, A. Arbabi, P. N. Petrov, E. Arbabi, S. Saurabh, A. Faraon, and W. E. Moerner, "Removing orientation-induced localization biases in single-molecule microscopy using a broadband metasurface mask," Nat. Photonics **10**(7), 459–462 (2016).
52. A. E. Minovich, A. E. Miroshnichenko, A. Y. Bykov, T. V. Murzina, D. N. Neshev, and Y. S. Kivshar, "Functional and nonlinear optical metasurfaces," Laser Photonics Rev. **9**(2), 195–213 (2015).
53. H. Husu, R. Siikanen, J. Mäkitalo, J. Lehtolahti, J. Laukkanen, M. Kuittinen, and M. Kauranen, "Metamaterials with tailored nonlinear optical response," Nano Lett. **12**(2), 673–677 (2012).
54. N. Segal, S. Keren-Zur, N. Hendler, and T. Ellenbogen, "Controlling light with metamaterial-based nonlinear photonic crystals," Nat. Photonics **9**(3), 180–184 (2015).
55. K. O'Brien, H. Suchowski, J. Rho, A. Salandrino, B. Kante, X. Yin, and X. Zhang, "Predicting nonlinear properties of metamaterials from the linear response," Nat. Mater. **14**(4), 379–383 (2015).
56. G. Li, S. Chen, N. Pholchai, B. Reineke, P. W. H. Wong, E. Y. B. Pun, K. W. Cheah, T. Zentgraf, and S. Zhang, "Continuous control of the nonlinearity phase for harmonic generations," Nat. Mater. **14**(6), 607–612 (2015).
57. J. W. Goodman, *Statistical Optics* (John Wiley & Sons, 2000).
58. B. Perez-Garcia, A. Yepiz, R. I. Hernandez-Aranda, A. Forbes, and G. A. Swartzlander, "Digital generation of partially coherent vortex beams," Opt. Lett. **41**(15), 3471–3474 (2016).

1. Introduction

Light manipulation devices for frequency, phase, amplitude, polarization and orbital angular momentum (OAM) which are based on different physical phenomena, are generally limited in the strength of the light-matter interaction, with conversion efficiency $\eta \ll 1$ as depicted in Fig. 1(a). Incorporating such devices into a laser cavity, can effectively enhance their interaction with light, and thus overcome this limitation. For example, low efficiency frequency conversion elements have been integrated inside a laser cavity as an output coupler to achieve effective efficiency of $\eta_{\text{eff}} \approx 1$, depicted in Fig. 1(b) [1]. Nanophotonic devices such as metasurfaces – metamaterials of reduced dimensionality – offer exciting novel opportunities for light manipulation, but often suffer from limited efficiency, especially for multifunctional devices [2]. To overcome this limited efficiency we incorporated nanophotonic metasurfaces into a laser cavity as an output coupler as illustrated in Fig. 1(c). By matching the conversion efficiencies of these metasurfaces to the optimum reflectivity of our laser (see Methods for details), we improved the effective efficiency of the elements, and achieved $\eta_{\text{eff}} \approx 1$.

Intra-cavity metasurfaces are good candidates to generate laser beams of different topologies that can be controlled by the intrinsic angular momentum of light – photon spin [3,4]. Moreover, shared-aperture multi-tasking metasurfaces can provide several independent desired output beams simultaneously, yielding multifunctional laser cavities. Incorporating metasurfaces inside laser cavities can also provide full control of the amplitude, phase, polarization and even spatial coherence of the self-consistent laser modes with higher fidelity and flexibility than the intra-cavity optical elements used so far [5–17].

Optics EXPRESS

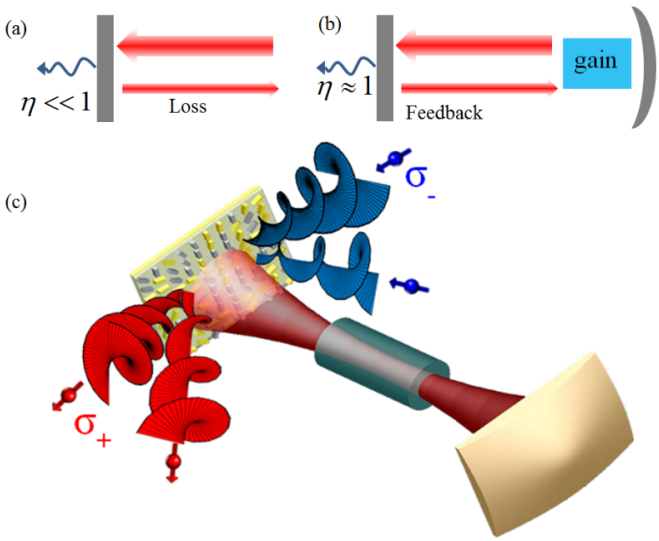

Fig. 1. Schematic of an intra-cavity multifunctional GPM and the spin-dependent ($\sigma \pm$) output beams of wavefronts with OAM. (a) Limited strength of light-matter interaction results in low conversion efficiency $\eta \ll 1$ when used outside a laser cavity. (b) After incorporation inside a laser cavity the effective efficiency rises to $\eta_{eff} \approx 1$. (c) Illustration of twisted laser beams of opposite helicities and OAMs (red and blue helix) emerging from the output coupler GPM; OAM values are of $l = -1, -2$ for σ_+ and $l = 1, 2$ for σ_-.

Metasurfaces consist of a dense assembly of resonant optical subwavelength nanoantennas. The light-matter interaction of such subwavelength structures allow substantial control of the local light scattering properties [2,18–32], and effective control of their electromagnetic response can be achieved by a geometric phase mechanism – Pancharatnam Berry phase, enabling spin-controlled phase modulation [19,20,33,34]. Geometric phase metasurfaces (GPMs) are composed of anisotropic nanoantennas that generate a local geometric phase delay, corresponding to the orientation function $\phi_g = 2\sigma\varphi\theta(x, y)$. Here, $\theta(x, y)$ is the in-plane nanoantenna orientation angle and $\sigma = \pm 1$ denotes the polarization helicity, i.e., right (σ_+) or left (σ_-) circular polarization, respectively. With geometric phase that utilizes spin-orbit interaction phenomenon [3,4], it is possible to obtain optical vortices with spin-controlled topological charges. Shared-aperture GPMs can generate multiple structured wavefronts, such as vortex beams carrying orbital angular momentum and optical vectorial vortices, by exploiting interleaving and harmonic response (HR) approaches. The interleaved metasurfaces are formed by randomly interspersing sub-arrays, resulting in a multi-tasking device with high flexibility [2,35,36]. Each sub-array is associated with a specific phase function, sparsely sampled at randomly chosen positions in the structure. Multiple distinct wave functions can be achieved by using the interleaving approach within a single shared-aperture, without reducing the numerical aperture of each sub-element. Additional shared-aperture technology can utilize the HR approach in which the phase function is expanded into harmonic orders [37,38].

2. Experimental results and discussion

Here we report on the incorporation of the shared-aperture GPM into a laser resonator to form spin-controlled twisted light beams with various OAM, as illustrated in Fig. 1(c). The GPMs, based on gap-plasmon resonance nanoantennas, were placed inside a modified degenerate cavity (MDC) with a Nd:YAG gain medium, which was effectively used in various applications and scientific investigations [39–41]. Such MDC laser allows flexibility for handling our small-area elements, and control of the spatial coherence properties (see

Optics EXPRESS

Methods for details). It consists of a back mirror, gain medium, two lenses in a *4f* telescope arrangement, and a GPM as an output coupler as presented in Figs. 2(a) and 2(b). The *4f* telescope arrangement assures that any field distribution is accurately imaged onto itself after a single roundtrip, and therefore any field distribution is an eigenmode of the cavity. We inserted a pinhole aperture at the Fourier plane between the two lenses inside the cavity, in order to filter out higher spatial frequencies (spatial modes).

We chose a small ~1mm intra-cavity pinhole aperture to select the lowest intra-cavity mode. To achieve spin-dependence, we added polarization control that enforced circular polarization $\sigma_{\pm}$ (see schematic in Fig. 2(b)). The spin-controlled lasing modes, which build up in the cavity were obtained by placing inside the cavity a polarizer, a Faraday rotator and a quarter waveplate (QWP). The QWP was oriented at either + 45° or –45° angles with relation to the direction of polarization of the incident beam, introducing high loss to the σ_{+} or σ_{-}. Only part of the beam traveling in the cavity interacts with the output coupler GPM and contributes to the spin-dependent laser output, while the rest of the beam is left unchanged and is reflected back into the cavity, where it contributes to future buildup of the lasing mode inside the cavity.

The GPM is based on gap-plasmon resonator (GPR) nanoantennas that consist of metal-insulator-metal layers (see schematic in Fig. 2(a), inset), enabling high reflectivity by increasing the coupling between the free-wave and the fundamental resonator mode. Moreover, adjustment of the GPR nanoantenna dimensions enables the design of a half-wave plate [25-26]. We fabricated a metasurface that is composed of a continuous SiO_2 film of 110nm sandwiched between a continuous gold substrate and gold nanobricks on top. The nanobricks, with dimensions of 210x70x30nm^3, are arranged in a square array with a lattice constant of 250nm to form the metasurface of 50μm diameter.

We demonstrated control of spin and OAM by placing an intra-cavity GPM in the MDC and generating a single OAM mode of $l = \pm 1$. In the design of such GPM, the GPR nanoantennas were oriented according to the relation $2\theta(x,y) = kx + l\varphi$, to obtain momentum redirection $\sigma_{\pm} k$ and topological charge $\sigma_{\pm} l$; φ is the azimuthal angle and $l = 1$. Figures 2(c) and 2(f) show the output beams from the two output channels of the cavity, and demonstrate that the laser can switch between the channels by changing the orientation of the QWP (+ 45° or –45°). The corresponding OAMs were determined by measuring the interference of each output beam with itself, using a Mach-Zehnder interferometer. The resultant fringe patterns at both output channels reveal two ”forks”, indicating a singularity of the field with topological charge of $l = \pm 1$ as shown in Figs. 2(g) and 2(h) where the direction of the forks indicates the sign of the OAM. The spin-controlled OAM results from the spin to orbital angular momentum conversion formed by the GPM.

Optics EXPRESS

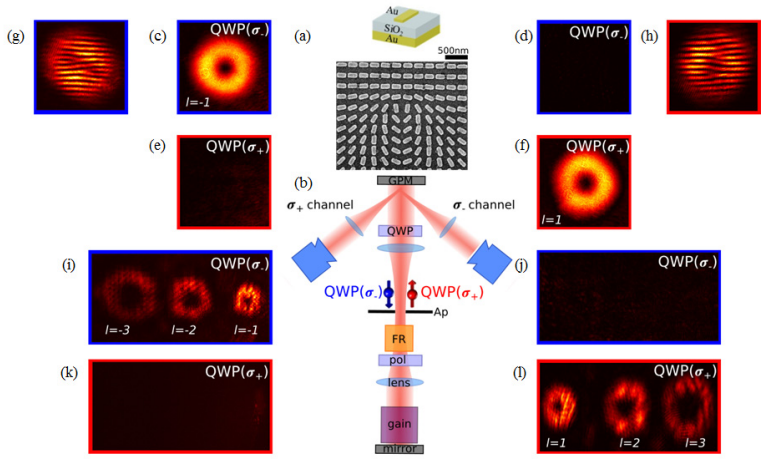

Fig. 2. Spin-controlled OAM output beams generated by intra-cavity GPM. (a) Scanning electron microscope image of the fabricated HR-GPM composed of gap-plasmon nanoantennas (inset). (b) Schematic of a twisted modified degenerate cavity laser. The output coupler of the standard cavity is replaced with a GPM, which is used to manipulate the properties of the laser output. The sign of the circular polarization of the mode that builds up inside the cavity is controlled with a polarizer (pol), a Faraday rotator (FR) and a quarter wave plate (QWP). Since the phase function of the GPM is spin-dependent, the output is switched between right and left channels by changing the orientation of the QWP. (c-f) Measured OAM outputs at the left (σ_+) and right (σ_-) channels of the twisted MDC laser with two orientations of the QWP($\sigma_\pm$). Red and blue squares correspond to helicity (σ_+ or σ_-, respectively) of the buildup mode polarization inside the laser cavity. (g, h) Self interference pattern of the output beam at the left and right channels, obtained with a Mach-Zehnder interferometer; the forks indicate OAM of $l = -1$ in the left channel, and OAM of $l = +1$ in the right channel, as expected. (i-l) Measured multiple harmonic helical output beams, generated by placing a spin-dependent HR-GPM of OAM with $l = \pm 1, \pm 2, \pm 3$.

Multiple harmonic output beams can be obtained by imprinting shared-aperture phase function onto the GPM. Accordingly, we designed a shared-aperture GPM based on the HR approach where the phase function is expanded according to $\exp[i\phi_g(x)] \cong \sum_m A_m \exp[im\sigma_\pm(kx + \varphi)]$, resulting in a finite number of dominant multiplexed OAM harmonic orders with identical intensities and with the momentum redirection of the m^{th} order. We adopted an optimized analytic solution [38] to realize a GPM that provides three spin-dependent asymmetric OAM harmonic orders. By forming such structures and placing them as spin-dependent output couplers in our MDC, Figs. 2(i)-2(l) show the obtained output beams with OAM of $l = +1, +2, +3$ for intra-cavity spin state σ_+ and $l = -1,-2,-3$ for intra-cavity spin state σ_-. The output coupling of the twisted MDC was found to be ~10%, intended to match the optimum output coupling of the Nd:YAG laser (see Methods for details). Accordingly, the amount of energy from the shared-aperture GPM is nearly equal to the maximum that could be generated by the laser. In our experiments, the measured effective efficiency of the shared-aperture GPM was 94% (see Methods for details), significantly higher than the reported efficiency of such elements, $\eta = 62\%$ [2]. The advantage of our method would be even more pronounced for more sophisticated elements, which are expected to suffer from even lower efficiencies.

By replacing the small intra-cavity pinhole aperture with a much larger one (10mm), we enable the existence of higher order spatial modes in the cavity, thereby decreasing the degree of spatial coherence [41] and generating partially coherent vortex beams [42,43]. Figure 3(a) shows the measured intensity distribution of the partially coherent vortex beam generated by the GPM of a single OAM of $l = 1$ (inset), and the experimental setup of a wavefront folding interferometer that was used to measure the spatial coherence of the output beam [41]. Note that no singularity is observed in the intensity distribution of the partially coherent vortex

Optics EXPRESS

beam. The measured spatial coherence, which is shown in Fig. 3(b), obtained with the wavefront folding interferometer indicates that the partially coherent vortex beam has a ring dislocation [42, 44] corresponding to $l = 1$, in agreement with the predicted result shown in Fig. 3(b) inset; see Methods for details. When placing the HR-GPM as an output coupler, we generated multiple partially coherent vortex beams of $l = 1,2,3$ from the MDC as shown in Fig. 3(c). In contrast to the results in Fig. 2(i) of multiple coherent vortices, the singularity in the first harmonic order is absent and the dark spot in the higher harmonics is relatively small due to the incoherency of the modes, Figs. 3(c)-3(e) shows the agreement with calculation. The manipulation of the spatial coherence with the partially coherent twisted MDC laser could be potentially exploited for speckle free stimulated emission depletion microscopy, metrology, target acquisition and optical coherence tomography.

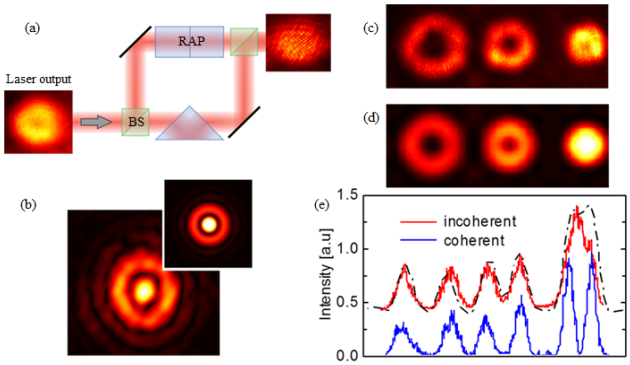

Fig. 3. Generation of partially coherent vortex beams. (a) The experimental setup of a wavefront folding interferometer for spatial coherence measurement; RAP – right angle prism (acts as a Dove prism); BS – beam splitter. Insets depict the intensity distribution of a partially coherent vortex beam generated by a GPM of $l = 1$ (lower inset, laser output), and the corresponding interference pattern (upper inset). (b) The resultant experimental spatial coherence function. Inset depicts the corresponding calculated coherence function. (c) Experimental intensity distribution of the laser output of multiple partially coherent harmonic vortex beams and (d) the corresponding calculation. (e) Cross sections of the experimental (red line) and calculated (black) intensity distributions of partially coherent vortices, and for fully coherent vortices (blue, taken from Fig. 2(i)).

An additional attractive feature of metasurfaces is based on space-variant polarization manipulation, which encompasses a broader class of wavefronts, particularly vectorial singular optics. Singularities in a scalar vortex, OAM wavefront, occur where the phase of the scalar wave has a spiral structure around a singular point in the field [45–47]. However, a space varying polarization enables the generation of vectorial vortices, which appear around the point where the polarization is either undefined or changes abruptly [48]. The formation of vectorial vortices is enabled by the coherent superposition of scalar vortices with opposite topological charges and spin states. Vectorial vortices are of great interest for optical communications, super-resolution, optical tweezers and laser beam shaping [6, 49–51].

The shared-aperture interleaved GPM enables superposition of twisted light beams via interleaving sparse antenna sub-arrays (see Fig. 4). These sub-arrays are randomly dispersed across the shared area of the GPM, so as to provide equal weight to each phase function and minimize diffractive artifacts. In order to achieve a phase profile for generating a vectorial vortex, we spatially multiplexed two phase functions generating opposite scalar vortices. In particular, for interleaved geometric phase profiles of $\phi_g^{(1)}(x, y) = \sigma_{\pm}(kx + l\varphi)$ and $\phi_g^{(2)}(x, y) = \sigma_{\pm}(-kx + l\varphi + \Delta\phi)$, the resulting vectorial field for incident light of linear polarization has the form $\exp[i(kx + l\varphi)]\ |\sigma_+\rangle + \exp[i(kx\text{-}l\varphi\text{-}\Delta\phi)]\ |\sigma_-\rangle$, where $|\sigma_{\pm}\rangle$ is the spin state, and $\Delta\phi$ is a constant geometric phase. For example, a superposition of in-phase ($\Delta\phi = 0$) and out-of-phase

Optics EXPRESS

($\Delta\phi = \pi$) scalar vortex beams with $l = \pm 1$ results in radial and azimuthal polarizations, respectively.

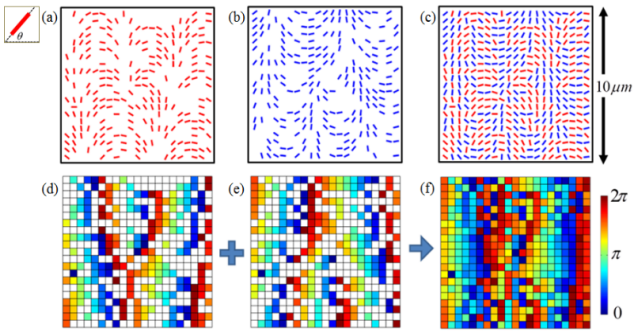

Fig. 4. Interleaved GPM concept. (a-c) Sub-array structures of $2\theta(x, y) = kx + l\varphi$ (a) 2θ(x, y) = $-kx + l\varphi$ (b) and the resultant interleaved GPM (c) for the generation of a radial vortex beam; $k = (2\pi/\lambda)\sin(10)$, $\lambda = 1064$ nm. The inset depicts the orientation angle θ. (d-e) The corresponding sparse geometric phase profiles for illumination with σ_+ (d) and σ_- (e), and the resultant interleaved geometric phase under linear polarization illumination (f); the color bar denotes the geometric phase from 0 to 2π.

We investigated vectorial vortices generated with an intra-cavity interleaved GPM, where the state of the output beams is controlled by the polarization of the mode in the MDC. By placing the GPMs inside a degenerate cavity with linearly polarized laser mode, we obtained radially and azimuthally polarized beams as shown in Fig. 5(a) and 5(b). In addition Fig. 5(c) shows the obtained vectorial vortex of winding number $l = 2$. The images of vectorial vortices which show the space-variant polarization states were obtained after a linear polarizer rotated in eight representative orientations. The polarization vector fields at the outputs were derived from the measurement of the Stokes parameters of the vectorial vortices (see upper insets in Fig. 5). The calculated deviation from the desired polarization orientation was 15°, and the average ellipticity angle was found to be 18°. Therefore, the overall polarization purity (percentage of power which is linearly vectorial vortex) was determined to be ~92%. The transformation from vectorial to scalar vortex beams can be obtained by modifying the polarization of the MDC mode to be purely circular instead of linear polarization (see Methods for details).

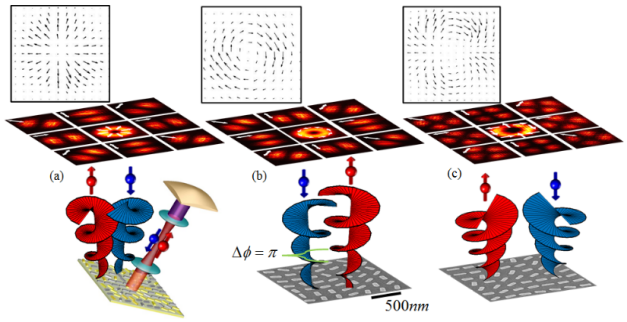

Fig. 5. Vectorial vortex output beams with different topologies. (a-c) Illustrations of the twisted output beams emerging from the intra-cavity GPM and the far-field measurements of radial polarization (a), azimuthal polarization (b), and vectorial vortex of winding number $l = 2$ (c), generated by a coherent superposition of wavefronts with opposite OAMs (red and blue helixes) and helicities σ_+ (red arrow) and σ_- (blue arrow); schematic (a) and SEM images (b, c) of the corresponding GPMs. Experimental polarization distributions were obtained by placing an external linear polarizer at eight different orientations, where the white arrows denote the space-variant polarization. Upper insets show the polarization vector fields of the output beams that were derived from the measurement of the Stokes parameters.

Optics EXPRESS

3. Concluding remarks

The incorporation of a multi-tasking metasurface based on the Pancharatnam-Berry phase mechanism, into a laser cavity enables control of the topology of the output beam in a spin-dependent manner and with enhanced efficiency. Intra-cavity GPM elements, composed of sub-wavelength phase modulating building-blocks, currently offer greater flexibility in manipulating multiple concurrent optical tasks than other intra-cavity elements, such as diffractive, phase and q-plate elements [7,12-13]. Specifically, they can serve as multifunctional intra-cavity elements, and can generate OAM beams with controlled spatial coherence. In addition, intra-cavity GPM elements can be naturally incorporated into micro-lasers, and can be easily integrated in nanophotonic devices. Our configuration where we incorporate metasurfaces into laser cavities can also be exploited with nonlinear nanophotonic devices, reconfigurable metasurfaces and graphene nanostructures [32, 52–56]. The shared-aperture intra-cavity GPM paves the way for the generation of multimodal singular wavefronts – twisted light beams having OAM and polarization singularity. We believe that the unique combination of novel intra-cavity GPMs with new configurations of laser cavities could lead to new and exciting applications that require arbitrary control of the properties of laser output light beams, and that are currently not possible.

4. Methods

A. Fabrication of GPM based on GPR nanoantennas

The GPR-based metasurfaces were fabricated using electron-beam lithography and a lift-off technique. On a SiO_2 substrate titanium adhesive thin film of 2nm, gold film of 300nm, and additional titanium film of 2nm were deposited by e-beam evaporation. Then a SiO_2 film of 110nm was grown above using a PECVD system. The e-beam lithography of the metasurface pattern using PMMA 950 A3 photoresist was performed, followed by e-beam evaporation of 2nm titanium and 30nm gold film, and subsequent lift-off procedure.

B. Modified degenerate cavity arrangement

The MDC consisted of two lenses with focal lengths of f = 150mm, a Nd:YAG gain medium of 10cm length and 4mm in diameter, a high reflective back mirror and the GPM as an output coupler (see Fig. 6). The diameter of the GPM elements was 50μm. The lasing area of the gain was limited by an aperture of 100μm in diameter. A pinhole aperture placed at the focal plane between the lenses serves as a spatial filter. Pinhole diameters varied between 0.4 mm to 10 mm. The *4f* telescope arrangement assures that any field distribution is accurately imaged onto itself after a single roundtrip, and therefore any field distribution is an eigenmode of the cavity. Since the cavity supports many different eigenmodes, the cavity can lase in many different modes simultaneously, despite mode competition. The operating output power of the laser in our experiments was ~200mW.

It is convenient to describe the modes near the mirror of the degenerate cavity as an incoherent sum of plane waves propagating in different angular directions. Each plane wave is then focused to a diffraction limited spot at the Fourier plane. By inserting a pinhole aperture at the Fourier plane between the two lenses inside the cavity, it is possible to limit the range of angles, and therefore filter out higher modes. Accordingly, increasing the size of the aperture is therefore equivalent to reducing the degree of spatial coherence of the MDC laser. Since the mode filtering is at the Fourier plane far from the gain medium, there is practically no reduction of the output power from the laser [40].

Optics EXPRESS

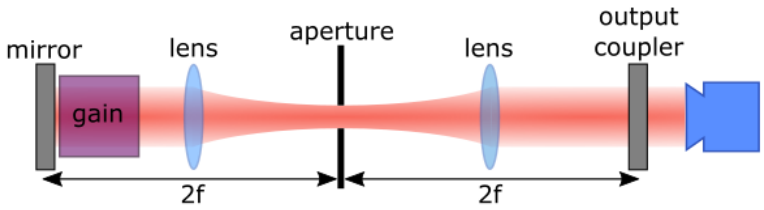

Fig. 6. Modified degenerate cavity (MDC) laser arrangements. The number of lasing modes is controlled by changing the size of an intra-cavity pinhole aperture.

C. Comparing intra-cavity to external GPM elements

The GPM elements placed outside a laser cavity have been extensively investigated in the past [2]. In this section we compare the results of the past investigations to the results obtained with GPM elements that are placed inside the laser cavity. For the comparison, we consider results with the multi-tasking shared-aperture GPM elements.

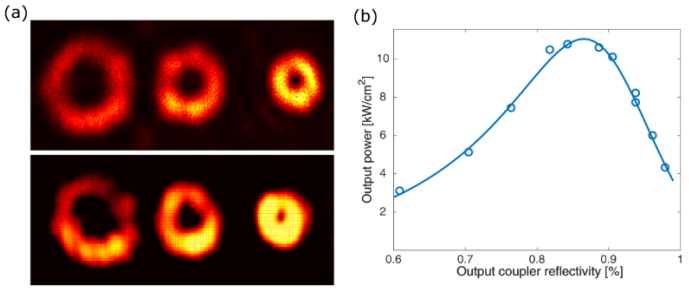

Fig. 7. Intracavity GPM and external GPM elements. (a) Experimental intensity distributions of the multi-tasking elements, when placed inside (top) and outside (bottom) a laser cavity. (b) Experimental output power as a function of output coupler transmittance. The total conversion efficiency of the GPM element was designed to match the optimum transmittance of the laser, around 12%. Due to fabrication and technical issues, the actual total conversion efficiency of the elements was 10%, closely matching the optimum output coupler transmittance.

We found that all orders of the shared-aperture GPM elements are excited, regardless of whether the GPM elements are placed outside or inside the twisted MDC laser as shown in Fig. 7(a). The intensity distribution and mode purity of the output beams are similar, in both cases. When placed outside the laser cavity, the purity of the Laguerre Gauss beams – defined as the normalized intensity overlap integral between the actual intensity distribution and expected intensity distribution – was measured to be 95.8%, 90.8% and 79.3% for l = 1, 2, 3, respectively, and when placed inside the laser cavity it was 95.5%, 89.5% and 87.8%, for l = 1, 2, 3, respectively. The dominant difference between the elements placed outside or inside the laser cavity is their effective efficiency. The efficiency of the HR GPM outside of the cavity was found to be $\eta = 62\%$ [2]. In order to achieve the optimum output coupling of the Nd:YAG laser of ~10% as depicted in Fig. 7(b), we designed the waist diameter (D_1) of the intra-cavity Gaussian mode that impinges the back reflector of the resonator to match the output coupler GPM of diameter D_2 according to the ratio $(D_1/D_2)^2 \sim 10\eta$. Here the back reflector was fabricated as a metasurface surrounded by a gold film. Consequently, when the multifunctional GPM was placed inside the laser cavity, its effective efficiency increased to 94%, indicating that the total power from GPM is close to the maximum power that could be generated by the laser cavity without the GPM element.

D. Measurement of the spatial coherence

The degree of spatial coherence is described by the complex coherence factor μ, defined as $\mu(x, y; x', y') = \langle E(x, y)E^*(x', y')\rangle_t$, where $E(x, y)$ denotes the field at point (x, y) and $\langle\bullet\rangle_t$ time averaging [57]. Generally, the complex coherence factor is a four dimensional function, μ =

Optics EXPRESS

$\mu(x, y; x', y')$. However, for an incoherent source the Van Cittert-Zernike theorem predicts that the complex coherence factor is really just a two dimensional function that depends only on the difference in coordinates, $\mu = \mu(x-x', y-y')$. Consequently, for an incoherent source, it is sufficient to measure the complex coherence factor only as a function of the difference in coordinates, and still obtain all information of the spatial coherence.

Figure 3 shows the experimental setup of a modified Mach-Zehnder interferometer (wavefront folding interferometer), which was used to measure the spatial coherence. There, the output image from the laser was split by a beam splitter and directed into the two arms of the interferometer. The image in each of the two arms was then flipped so that the relative orientation between the two images was rotated by 180° around the optical axis. The beams were recombined with a second beam splitter. A slight angle was introduced to the second beam splitter, so as to form a fringe pattern of the interference of the fields $E(x, -y)$ and $E(-x, y)$, which was detected by a CMOS camera. The visibility of the interference pattern $v(x, y)$ is equal to the absolute value of the complex coherence factor $\mu = \mu(x, y; x', y')$, according to the relation $v(x, y) = |\mu(-x, y; x, -y)| = |\mu(-2x, 2y)|$; and the relative location of the fringes indicates the phase of the complex coherence factor [57].

In order to calculate μ, we model the output of the twisted MDC as an incoherent sum of plane waves with OAM propagating in different angular directions, $E_{out} = \sum_{\alpha,\beta} E_l(r, \varphi) \exp[-ik_0 (\alpha r\cos\varphi + \beta r\sin\varphi)]$ where k_0 is the wavenumber, $E_l \sim A(r)\exp(il\varphi)$ and (α, β) determine the angular directions of the plane waves, the range of which depends on the pinhole aperture size, assuming small angles. Therefore, the intensity fringe pattern as detected by the camera is $I = \sum |E_{out}(r, \varphi) + E_{out}(r, \varphi + \pi)\cdot\exp(ik_0\gamma r\cos\varphi)|^2$, where γ is the angle introduced by the second beam splitter of the wavefront folding interferometer.

Figure 8 shows the experimental and calculated spatial coherence for a single vortex beam using a GPM of a single OAM of $l = 1$. The interference pattern of a partially coherent vortex beam as shown in Fig. 8(a) and, after applying straightforward Fourier analysis, the absolute value and the phase of the complex coherence factor as seen in Fig. 8(b). As evident, there is good agreement between the calculated and the experimental results.

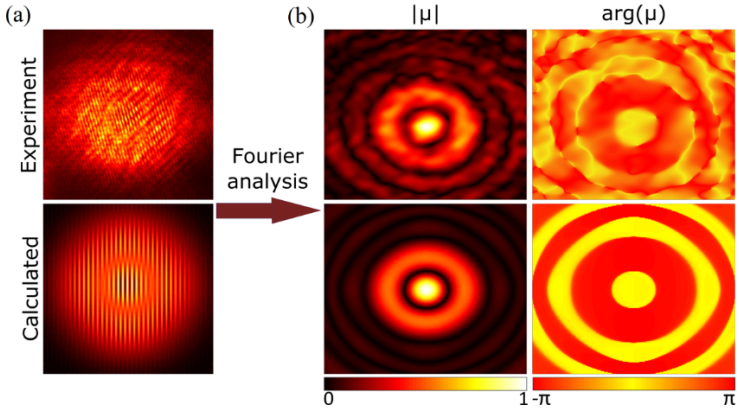

Fig. 8. Spatial coherence for a vortex beam using a GPM of a single OAM of = 1. (a) Calculated and measured intensity distributions at the output from the wavefront folding interferometer. (b) The calculated and measured amplitude and phase of the complex coherence factor (spatial coherence). The experimental results are in good agreement with calculated results.

The coherence length L_c of the partially coherent vortex can be calculated by $L_c = 0.61\lambda f/r$, where λ is the lasing wavelength, f is the focal length of the collimating lens after the laser cavity (see Fig. 2(b)) and r is the ring dislocation radius of $|\mu|$ [58]. The experimental coherence length, derived from Fig. 8(b), was found to be $L_c \sim 20\mu m$, which is close to the calculated coherence length [40].

Optics EXPRESS

E. Wavefront folding interferometer arrangement

The output of the MDC laser was collimated with a lens of f = 40mm focal length. The collimated beam was spilt into two arms of the interferometer, and inverted by right angled prisms, $x \rightarrow -x$ in one arm and $y \rightarrow -y$ in the other, and then recombined to form an interference pattern which was imaged onto a CMOS camera with a *4f* imaging telescope (f_1 = 150mm, f_2 = 100mm).

F. Spin-controlled transformation from vectorial to scalar vortex

The peculiarity of the geometric phase is based on its geometric nature. Unlike diffractive and refractive elements, it does not arise from optical path differences but from a space-variant manipulation of the light polarization state [19–21, 33]. The GPMs are formed by tiling a metasurface with anisotropic nanoantennas, arranged according to a desired space-variant orientation profile $\theta(x, y)$. A GPM transforms an incident circularly polarized light into a beam of opposite helicity, imprinted with a geometric phase $\phi_g = 2\sigma_{\pm}\varphi\theta(x, y)$. Consequently, for an arbitrary incident polarization state $|E_{in}\rangle$, the field emerging from a space-variant half-wave plate is $|E_{out}\rangle \propto \exp[i2\theta(x, y)]\ \langle\sigma_-|E_{in}\rangle|\sigma_+\rangle + \exp[-i2\theta(x, y)]\ \langle\sigma_+|E_{in}\rangle|\sigma_-\rangle$, where $|\sigma_{\pm}\rangle$ stands for the spin state, and $\langle\alpha|\beta\rangle$ denotes the inner product (46). Figure 5 in the main text shows the generation of vectorial vortices from interleaved GPMs under linear polarization illumination $|E_{in}\rangle = (|\sigma_+\rangle + |\sigma_-\rangle)/\sqrt{2}$, which result from the coherent superposition of wavefronts with opposite OAMs and spin states: $|E_{out}\rangle \propto \exp(il\varphi)\ |\sigma_+\rangle + \exp(-il\varphi)\ |\sigma_-\rangle$. The transformation from vectorial to scalar vortex beams is obtained by illuminating the interleaved GPM (see Fig. 5) with circularly polarized light via the spin-dependent MDC as depicted in Fig. 2(b), resulting in $|E_{out}\rangle \propto \exp(il\varphi)\ |\sigma_+\rangle$ or $|E_{out}\rangle \propto \exp(il\varphi)|\sigma_-\rangle$ for incident $|\sigma_-\rangle$ or $|\sigma_+\rangle$, respectively. Verification of the circular polarization state of the emerged beams is established by projecting these scalar vortices on linear polarizers at different orientations resulting in similar intensity profiles (see Fig. 9).

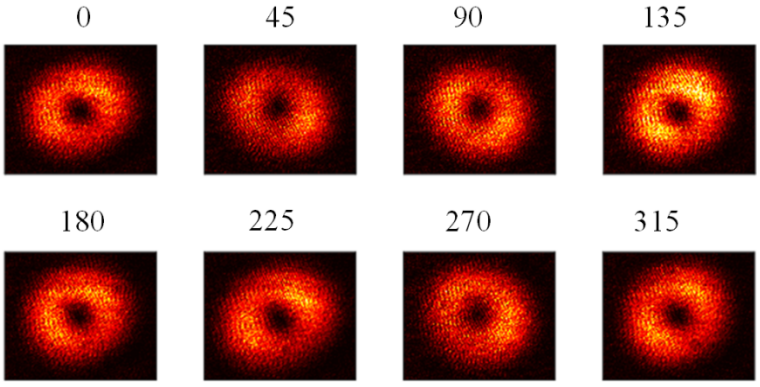

Fig. 9. Polarization analysis of the detected transformation from vectorial to scalar vortex. The numbers above each measurement denote the angular orientations of the linear polarizer.

Funding

Israel Ministry of Science, Technology and Space (3-11838); Israel Science Foundation (ISF) (1004/16); KLA-Tencor.

Acknowledgments

The fabrications of the metasurfaces were performed at the Micro-Nano Fabrication & Printing Unit (MNF&PU), Technion.